ORIGINAL ARTICLE

Additive Fabrication of a Vascular 3D Phantom for Stereotactic Radiosurgery of Arteriovenous Malformations

Elisa Legnani,[1,2,*] Pasqualina Gallo,[3,†,*] Federico Pezzotta,[1,i] Francesco Padelli,[3] Giuseppe Faragò,[3,‡]
Andrea Gioppo,[3] Lorenzo Gentili,[1] Elena De Martin,[3] Maria Luisa Fumagalli,[3] Francesco Cavaliere,[1]
Maria Grazia Bruzzone,[3] Paolo Milani,[1] and Tommaso Santaniello[1,ii]

Abstract

In this study, an efficient methodology for manufacturing a realistic three-dimensional (3D) cerebrovascular phantom resembling a brain arteriovenous malformation (AVM) for applications in stereotactic radiosurgery is presented. The AVM vascular structure was 3D reconstructed from brain computed tomography (CT) data acquired from a patient. For the phantom fabrication, stereolithography was used to produce the AVM model and combined with silicone casting to mimic the brain parenchyma surrounding the vascular structure. This model was made with tissues-equivalent materials for radiology. The hollow vascular system of the phantom was filled with a contrast agent usually employed on patients for CT scans. The radiological response of the phantom was tested and compared with the one of the clinical case. The constructed model demonstrated to be a very accurate physical representation of the AVM and its vasculature and good morphological consistency was observed between the model and the patient-specific source anatomy. These results suggest that the proposed method has potential to be used to fabricate patient-specific phantoms for neurovascular radiosurgery applications and medical research.

Keywords: additive manufacturing, stereolithography, tissue-equivalent materials, anthropomorphic phantoms, surgical applications

Introduction

PATIENT-SPECIFIC ANATOMY information deriving from computed tomography (CT) and magnetic resonance imaging (MRI) has substantially improved in the past few years, thanks to the development and refinement of medical imaging technologies and techniques.[1] Further addition of advanced image postprocessing tools allows to obtain accurate three-dimensional (3D) reconstructions of clinical cases, which are useful in both diagnosis and treatment planning.[2]

Stereotactic radiosurgery (SRS) is a radiation therapy technique used in the treatment of benign and malignant intracranial lesions.[3] In SRS, highly precise targeted X-ray radiation is delivered in only a single or few high-dose fractions to treat the tumor or the abnormality while preserving the surrounding healthy tissues.[4] For this purpose, 3D imaging is mandatory to correctly identify lesions in the brain and to define their exact size and morphology.[5–7] A relevant clinical case that can be treated with SRS is brain arteriovenous malformation (AVM).[5]

[1]CIMAINA and Department of Physics, University of Milano, Milan, Italy.
[2]Direct3D, Milan, Italy.
[3]Fondazione I.R.C.C.S. Istituto Neurologico Carlo Besta, Milan, Italy.
†Current affiliation: Radiotherapy and Radiosurgery Department, Humanitas Clinical and Research Center, Rozzano, Milan, Italy.
‡Current affiliation: Neuroradiology Department, Papa Giovanni XXIII Hospital, Bergamo, Italy.
*These authors contributed equally to this study.
iORCID ID (https://orcid.org/0000-0002-0140-1346).
iiORCID ID (https://orcid.org/0000-0003-1029-0307).

Opposite page: Cloud-to-mesh analysis comparing the 3D model of a patient-specific brain arteriovenous malformation phantom with the patient source anatomy, both reconstructed from computed tomography scans.
Image credit: Interdisciplinary Centre for Nanostructured Materials and Interfaces (CIMAINA), Physics Department, University of Milan and Fondazione I.R.C.C.S. Istituto Neurologico Carlo Besta, Milan, Italy.

AVM is a tangle of abnormal blood vessels affecting the bloodstream in the brain, causing a quick and direct blood flow from arteries to veins without the support of the network of smaller vessels and capillaries, bypassing the release of nutrients to the brain tissues and the removal of CO_2.[8] AVM can get progressively larger over time as the amount of blood flowing through it increases, forcing the heart to work harder to keep up with the extra blood flow. The resulting tangle of blood vessels, often called a nidus, can be extremely fragile and prone to bleeding because of the direct connections between high-pressure arteries and low-pressure veins.

Patient-specific phantoms are useful tools for the pre-planning of surgical treatments.[9] Phantoms are physical models recapitulating the morphology of the target anatomy and the radiological response of human tissues.[9,10] These anthropomorphic systems can be used to optimize the clinical treatment planning, to reduce the invasiveness on the patient's healthy tissues and minimize radiation dose.[10] Moreover, they can be employed for quality assurance (QA), dosimetry assessments, and for optimization of contrast media formulation. These models can also be helpful in establishing a better comprehension of the abnormality morphology as well as its configuration, orientation, and dimension.[9–12]

Additive manufacturing enabled the possibility to fabricate 3D models directly from medical imaging data, allowing an easier and one-step fabrication of complex shaped objects with fine resolution.[9] The realization of patient-specific 3D phantoms has huge potentials in various fields of medicine, including radiological activities, personalized radiotherapy treatments, and medical research.[12,13] A key feature to select a fabrication approach in relation to a particular clinical case is the response of the tissue-mimicking materials under CT scans, which is strongly dependent on their electron density, relative electronic density (rED).[11] The difference in the electronic properties translates into different X-ray attenuation.[14]

Variations in materials' radiodensity generate a gray scale map in the registered images. Water-equivalent materials (with rED ~ 1, such as thermoplastics and silicones) mimic the response of soft tissues (e.g., brain matter),[15,16] whereas bone-equivalent materials (rED ~ 1.5–2, typical of high-density polymers, such as polytetrafluoroethylene [PTFE]) mimic that of hard parts.[17,18]

The design and fabrication of cerebral vascular phantoms using additive manufacturing for neurosurgery have already been reported in the literature.[13,19–22] The most representative examples are mainly related to surgical aid applications (e.g., aneurysm clipping[20,23]) as well as to diagnosis,[24,25] blood circulation analysis,[26,27] and patients' information purposes.[12] The manufacturing strategies explored included material extrusion of thermoplastic polymers (e.g., fused filament fabrication [FFF][20,28]), VAT photopolymerization,[29,30] PolyJet printing,[31,32] and sacrificial approaches combining FFF of acrylonitrile butadiene styrene (ABS) templates and casting of silicone-based materials.[33,34]

In the SRS domain, a 3D morphofunctional phantom embedding the vascular structure of a patient-specific AVM would be of great importance.[6] To date, physical phantoms replicating the structure of the AVM have been realized only by producing solid models of the abnormality by means of stereolithography (SLA) and PolyJet printing, targeting at a better comprehension of the cerebrovascular anatomy and blood flow dynamics.[5,28,35,36] No examples of a hollow vascular 3D model replicating the AVM complexity, tissue radiological properties, and its relation to the contiguous brain parenchyma has been reported.

In this study, we present a simple yet effective methodology for manufacturing a realistic cerebrovascular phantom for SRS that resembles the morphology and configuration of a patient-specific AVM. The vascular structure was 3D reconstructed from brain CT scans acquired from a selected patient. We combined SLA to produce the hollow AVM model and silicone casting to mimic the brain parenchyma surrounding the vascular structure, using tissue-equivalent materials. The AVM of the phantom was filled with a contrast agent usually employed on patients for CT scans and the radiological response of the phantom was tested and compared with the clinical case.

The constructed model demonstrated to be a very accurate physical representation of the AVM and its vasculature. Furthermore, good agreement was observed between the model and the patient-specific source anatomy. These results suggest that the proposed method has potential to be used to produce patient-specific phantoms for stereotactic treatments preplanning, evaluation of contrast uptake in small blood vessels, and QA assessments.

Materials and Methods

Vascularized phantom design and fabrication: rationale and methodologies

AVM vascular phantom was designed and fabricated according to the workflow reported in Figure 1 and summarized as follows. A 3D model of the abnormality was reconstructed from patient's computed tomography angiography (CTA) scans (Fig. 1A), acquired using a single source double energy computed tomography (DECT) with rapid kilovolt peak switching (GSI Revolution CT, GE Medical Systems, Milwaukee, WT). The acquisition parameters were those applied in the clinical protocol of the authors' institution for anatomical study of AVMs (namely 120 kVp, 200 mA, and 0.625 slice thickness). The patient has signed a written consent to the Privacy together with the agreement to the use of data for research purpose according to standard clinical practice. All the necessary anonymized DICOM data were made available by the hospital institution for 3D printing and scientific research purposes. More details on the scanning spectral parameters are reported in the Supplementary Data (Section S1, Table S1). The axial images of the CTA scan were then exported to a specialized GE workstation (AWserver®) for postelaboration by an experienced interventional radiologist.

Angiographic images of the patient were also exported to the AWserver (Fig. 1B), to provide the radiologist with dynamic information on the blood vessels with particular attention to the main feeding arteries and draining veins. Combining anatomical and dynamic imaging, the radiologist identified the AVM volume and isolated it from other vascular structures (Fig. 1C). The so segmented volume constituted the 3D model of the pathological abnormality and was converted to an stl file with a specific tool available in the workstation.

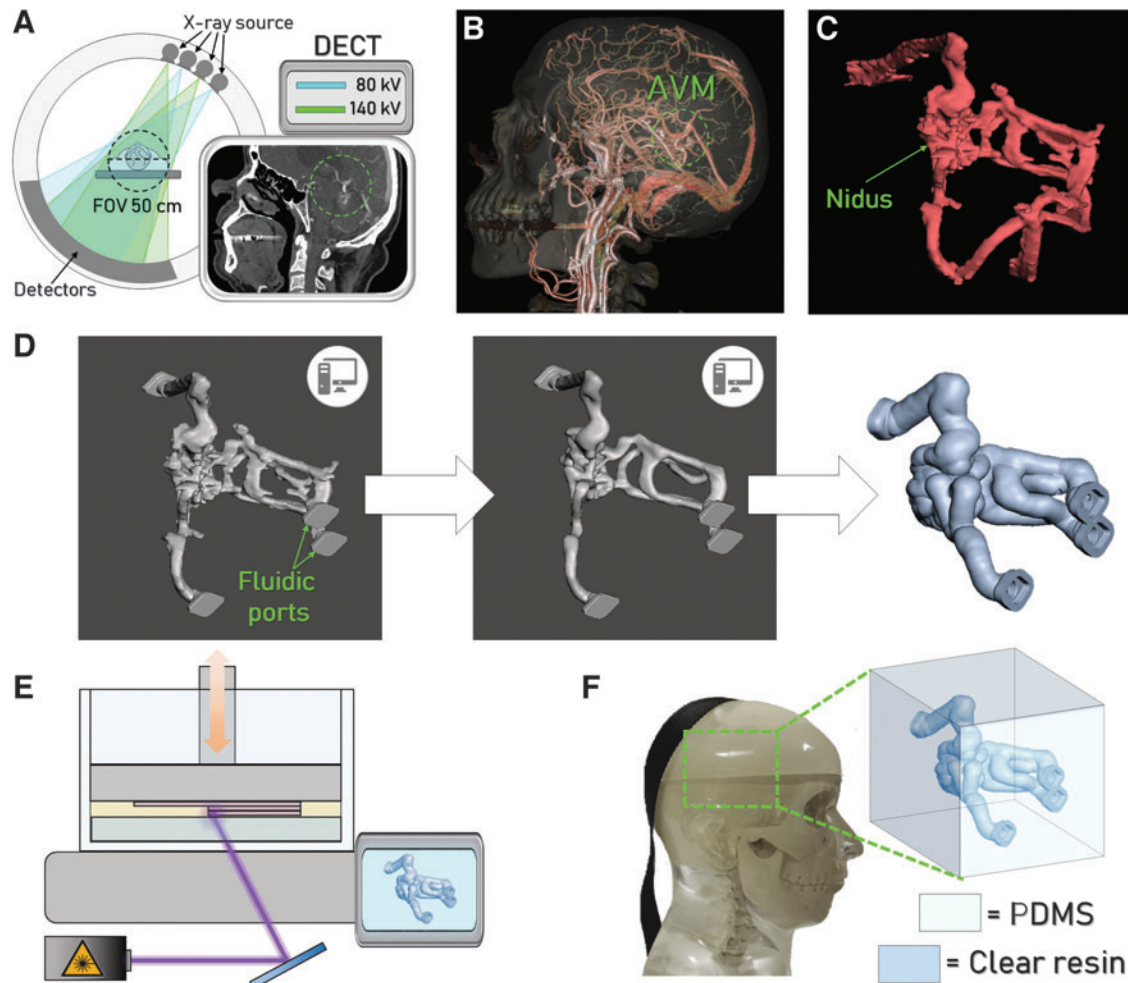The stl file of the AVM 3D model was then imported in MeshMixer® and refined to smooth/remove imaging edge

FIG. 1.   Workflow adopted for the vascular phantom realization. **(A)** Schematic illustration of the DECT scanner employed for CT imaging and a representative image acquired. The *green circle* highlights the presence of the AVM. **(B)** 3D rendering elaborated from CT images, used to identify and isolate the AVM (*green circle*) from the surrounding anatomical structures. **(C)** 3D solid model of the AVM and **(D)** 3D model elaboration using MeshMixer® to obtain the hollow AVM. **(E)** Schematization of the printing process to produce the physical model of the vascular AVM. **(F)** Representation of the complete phantom constituted by the AVM embedded into the silicone-based cube, fitting the commercial anthropomorphic phantom. 3D, three-dimensional; AVM, arteriovenous malformation; CT, computed tomography; DECT, double energy computed tomography.

artifacts. More specifically, after importing the model in the software, the first operation was to inscribe the AVM into a cube of the chosen dimension keeping the original structure orientation in space. Fluidic ports (previously designed using Fusion®) serving as inlets and outlets for contrast media injection using commercial syringes were imported in the stl format and joined to the AVM using the function Boolean union. After this, imaging edge artifacts, identified as spikes along the model contour, were eliminated using the separate and cut tools, and the AVM model was then refined and smoothed using manual flattening by means of the software brush modality. Several vascular structures were also suffering from imaging artifacts, appearing flattened in the model. After the input of the interventional radiologists, we used again the brush tool to slightly round them along the cross section. An automatic correction of minor defects (e.g., small-sized regions being left separated from the model surface after the elaboration) was then performed.

The shell around the model was generated using the offset function and the fluidic ports were subsequently obtained by cutting it at the interception points between the source model and the shell structure. The offset around the cavity was set at 1.8 mm. Images of the model refinement process are shown in Figure 1D. This model was then printed by means of SLA with a Form 2 machine (FormLabs) using the FormLabs Clear transparent resin (Fig. 1E). The AVM wall thickness was selected to ensure a tight interlocking between the supporting structures and the printed part (the penetration depth of the supports into the workpiece is 0.7 mm) and to confer an appropriate mechanical stability to the phantom for a safe handling and processing (e.g., to facilitate the support removal).

The SLA-printed AVM model was inserted into a cubic box serving as a mold for polydimethylsiloxane (PDMS) casting and curing. This silicone-based material was used to reproduce the brain parenchyma around the AVM. The radiodensities of both the resin and PDMS adequately represent the target anatomical structures in terms of tissue equivalence, as assessed using a dedicated protocol (details in the next section). The dimension of the PDMS component

embedding the AVM was set as $50 \times 50 \times 50$ mm to fit into an anatomically realistic head support, employed for radiosurgery QA (Fig. 1F) of the Cyberknife radiosurgery system (Accuray Sunnyvale, CA).

The complete system was then validated by filling the AVM with a contrast medium typically employed on patients and performing CT scans on the phantom encased in the head support, to obtain a 3D reconstruction of the AVM from the images acquired for comparison with the native patient's anatomy.

Tissue-equivalent materials selection

We first characterized the Clear resin and PDMS tissue equivalence using the Revolution GSI CT scanner to quantitatively estimate the polymers electron density relative to water (rED) starting from the registered gray scale levels and corresponding CT numbers (in Hounsfield units [HU]). We interpolated a calibration curve using data acquired from CT scans performed on a standard cone beam computed tomography (CBCT) Electron Density Phantom (Computerized Imaging Reference Systems) provided with biological tissue inserts at known electron densities (Fig. 2). The samples of the materials to analyze were then scanned in the same conditions.

We fabricated cylindrical components (25 mm diameter and 10 mm height) of both the Clear resin and PDMS that fitted into the CBCT phantom. CT scans were performed using the following parameters: 120 kV, 400 mAs, and 1.25 mm slice thickness with 30% iterative reconstruction. The CT central slice was chosen as the input for a MATLAB (MathWorks) custom-made script to define a circular region of interest (ROI) on the sample and calculate its mean pixel value and standard deviation. Using the calibration curve and the gray level obtained from CT imaging of the test materials, the rED values of the Clear resin and PDMS were computed and compared with that of brain matter.

AVM manufacturing

We used SLA to fabricate the AVM vascular model employing the Clear resin and a desktop Form 2 machine (FormLabs). This system is a classical SLA printer equipped with a 405 nm wavelength laser (250 mW) directed onto a computer-controlled mirror that deviates the ultraviolet (UV)

light into the resin tank to cure the liquid locally (laser spot size is 140 nm). The built platform lowers on the tank at a determined layer height to process one cross section of the part at the time. A transversal wiper operates at the top of the resin tank between each layer fabrication. This process is repeated until object completion.

Printing parameters for AVM manufacturing were set using the software PreForm®. Layer height was set to 0.1 mm. This value was selected to guarantee good dimensional accuracy of the printed part and relatively short fabrication timing. The orientation of the part with respect to the printing plate was carefully selected using a trial-and-error approach to avoid the use of supports into the hollow structure. The fabrication required ~4 h. The printed object was then immediately immersed in an isopropyl alcohol bath for 20 min to rinse it from any residuals of liquid resin. Vessels were thoroughly cleansed to prevent their obstruction. After complete washing, the AVM model was cured in a dedicated UV chamber at 60° for 30 min. These exposure time and postcuring temperature enable the completion of the polymer cross-linking without thermally stressing the material.

The obtained part is shown in Figure 3A. Supports were manually removed with a plier at the end of the process to obtain the final vascular structure (Fig. 3B, C). We chose to use the Clear resin because of its accuracy in reproducing small features and because of the material optical properties. In fact, the translucent appearance of the printed parts enables the operator to evaluate qualitatively the phantom filling after the injection of colored dyes and contrast media.

Silicone casting

The SLA-printed AVM model was inserted into a $50 \times 50 \times 50$ mm cubic box fabricated in ABS (natural, from OrbiTech) by means of FFF using a DeltaWASP 2040 printer, equipped with a 0.4 mm diameter nozzle. The inner volume of the printed box was exposed to acetone vapors for 30 min at room temperature to smooth the surface roughness of the walls to enhance the phantom transparency after PDMS casting. PDMS is a physically cross-linked elastomer widely employed for the realization of fluidic and microfluidic devices, due to its excellent physicochemical properties such as high thermal and chemical stability,
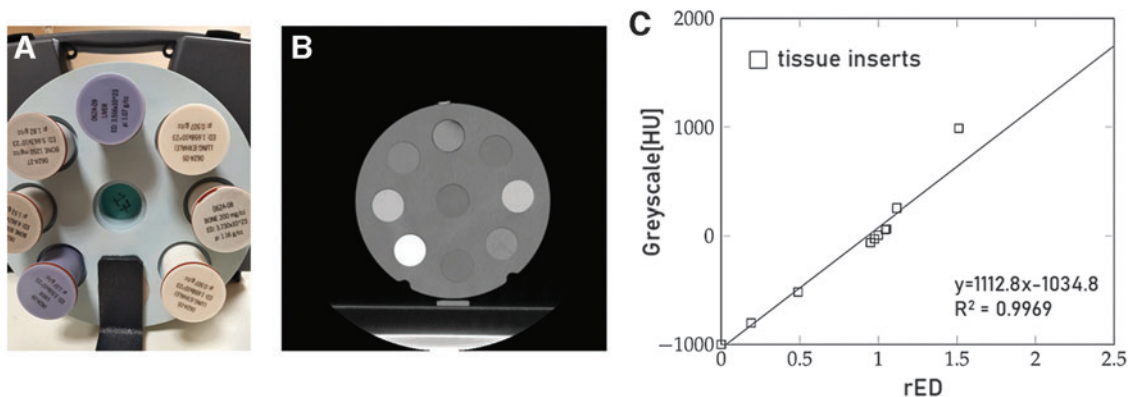

FIG. 2. **(A)** Picture of the CBCT Electron Density Phantom employed to generate the calibration curve for the assessment of the test materials' tissue-equivalence. **(B)** A CT scan of the phantom. **(C)** Calibration curve relating the standard inserts rED and CT numbers (WL 46, WW 1068). CBCT, cone beam computed tomography; CT, computed tomography; rED, relative electronic density.

FIG. 3. **(A)** AVM model straight after printing and **(B)** after removal of supports. **(C)** AVM filled with an aqueous solution containing a blue dye. AVM, arteriovenous malformation; CT, computed tomography.

biocompatibility, optical transparency, and high ability to replicate in detail solid structures with a resolution down to fractions of microns.[37,38]

PDMS was prepared using an elastomer-to-curing agent ratio equal to 10:1 w/w. The two compounds were mixed into a suitable beaker and degassed according to standard preparation protocols. The total volume of the polymeric solution was ~130 mL, slightly larger than the amount necessary to completely fill the 3D mold (total volume of the phantom was 120 mL, as calculated from the digital model). The mold was then filled with PDMS and degassed in vacuum for 3 h to ensure the complete removal of air bubbles. After that, it was heated at 50°C for 3 h and left at room temperature for 48 h until complete cross-linking in mild conditions (low temperature, long curing time). We point out that the PDMS curing condi-

tion could be optimized to shorten the curing time down 6 to 8 h using a low-temperature range between 65°C and 80°C. With these conditions, given the refined AVM 3D model, the total timing for the phantom fabrication is, therefore, 12 to 16 h.

Phantom validation

The radiological response of the phantom was tested and compared with the patient-specific anatomy. A preliminary DECT acquisition was performed by inserting only the AVM in a water bath. This operation was performed leaving the AVM empty to verify that all the vessels were connected and that the vascular structure presented no obstructions. To ensure the fluidic sealing of the system, suitable lids fitting the fluidic ports of the vascular structure were inserted. These
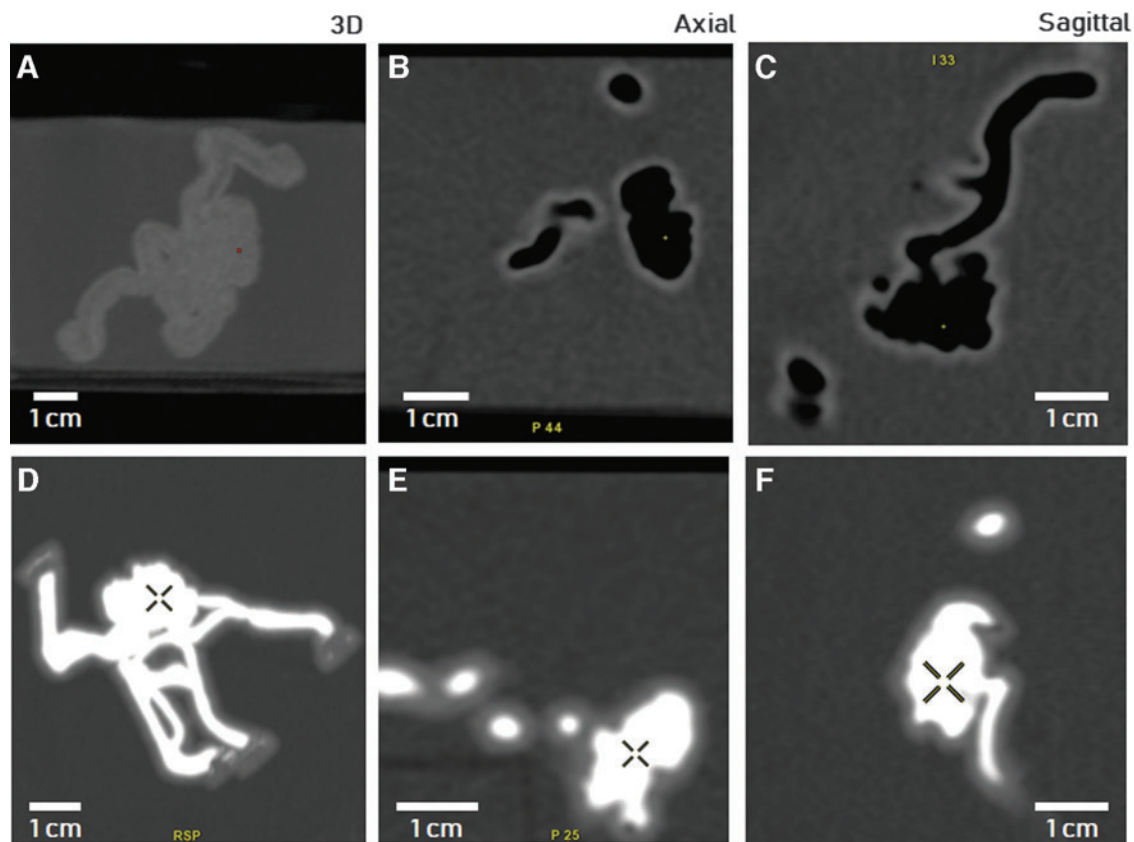

FIG. 4. 3D reconstruction, axial and sagittal CT scans of the SLA-printed phantom sealed with lids and immersed into a water vat. In **(A)** to **(C)** the phantom was empty, whereas in **(D)** to **(F),** it was filled with the contrast agent solution. CT, computed tomography; SLA, stereolithography.
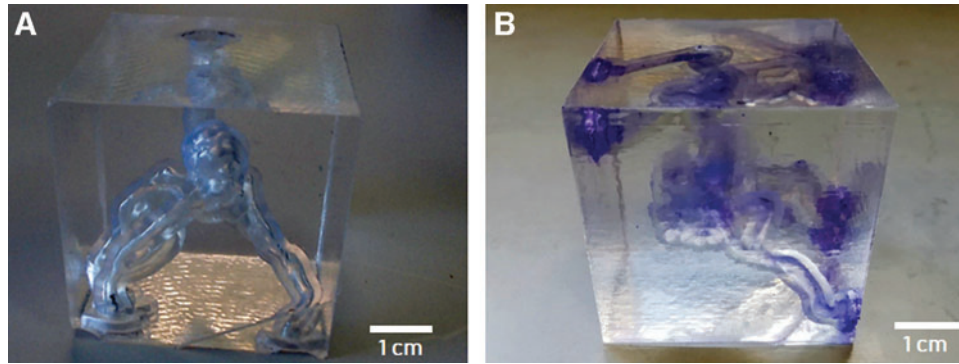
FIG. 5.   **(a)** AVM model printed with SLA and embedded in PDMS without **(A)** and with **(B)** the presence of the contrast agent in the vessels. AVM, arteriovenous malformation; CT, computed tomography; PDMS, polydimethylsiloxane.

were manufactured by means of FFF using hydrogenated styrenic block copolymer. Successively, the AVM phantom was filled with a contrast agent (Iopamiro® 370 mg/mL, Bracco Imaging S.p.A.) and demineralized water solution, with an iodine concentration of 35 mg/mL. The filling was carried out by immersing the phantom in the solution and by applying suction at the fluidic ports using a 10 mL syringe. A colorant was added in the solution to visualize the liquid inside the phantom and to qualitatively assess its filling.

The 3D model with the AVM embedded into PDMS was then CT scanned after implementation into the commercial anthropomorphic phantom. This phantom is designed for radiosurgery QA and resembles the X-ray attenuation prop-

erties and radiographic response of the corresponding human cranial anatomy. It is provided with a housing that accommodates a commercial Ball Cube, consisting of a plastic box encasing a pair of orthogonal radiochromic films and two plastic spacers. We replaced the series plastic box of the Ball Cube with our AVM phantom positioned into a dedicated box to carry out the system imaging.

All CT scans were performed using a volume CT dose index (CTDI$_{VOL}$) of 72.32 mGy compatible with radiosurgery acquisitions, whereas the slice thickness was set as 0.625 mm. The field of view was 30 cm. The CT images acquired were then transferred to the AWserver workstation for analysis. Two board-certified interventional radiologists
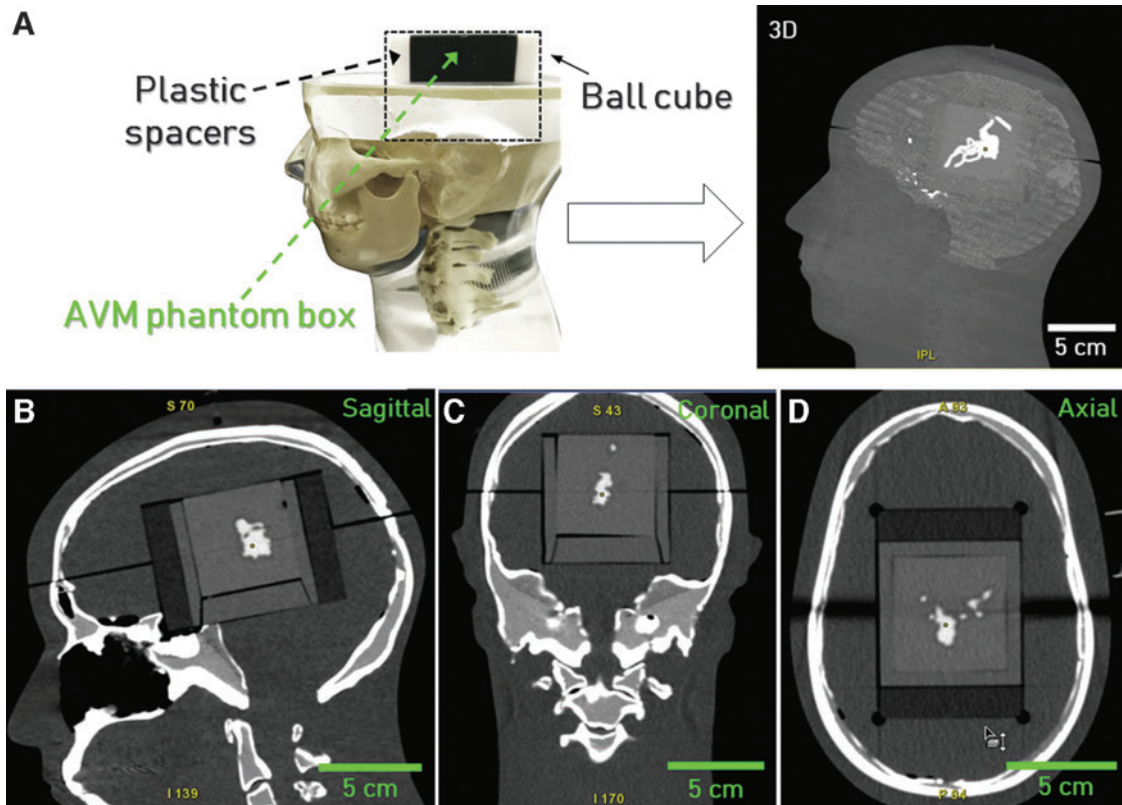

FIG. 6.   **(A)** Experimental setup for the validation of the AVM phantom embedded in PDMS filled with the contrast agent and fitted into the anthropomorphic phantom. **(B)** Sagittal, **(C)** coronal, and **(D)** axial CT scans of the phantom. AVM, arteriovenous malformation; CT, computed tomography; PDMS, polydimethylsiloxane.
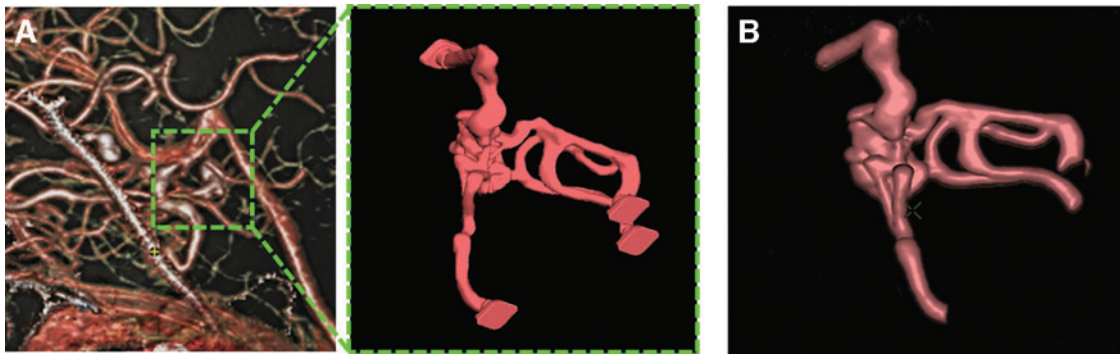
FIG. 7.   **(A)** AVM structure of the patient, isolated, modeled, and postprocess directly form CT images compared with **(B)** the 3D reconstruction of the AVM elaborated from CT data acquired using our phantom. AVM, arteriovenous malformation; CT, computed tomography.

independently assessed images using the proprietary image viewer. They were blinded to the type of lesion and were free to adjust window settings.

Results

The radio-opacity of both PDMS and Clear resin was successfully assessed. We obtained quantitative information on the materials' radiological properties using the calibration curve shown in Figure 2 and specifically comparing the polymers' radiodensity with that of the brain soft tissue. The obtained values of rED for PDMS and Clear resin were 1.087 and 1.038, respectively. Compared with the brain rED (1.01), the obtained values showed a discrepancy ΔrED of 2.8% and 7.6% for the Clear resin and PDMS, respectively, and, therefore, the two materials could be considered suitable candidates to mimic the soft tissues of interest. The results of this analysis are also consistent with what is reported in the literature concerning the water equivalence of silicone-based materials and photopolymers in terms of gray levels.[39–41] With our approach, the tissue equivalence of the polymers could be established by correlating the radio-opacity of the materials with the main physical property determining their radiological behavior.

CT images of the AVM phantom immersed in the water bath are shown in Figure 4. Although panels 4A–C show the empty AVM model, panels 4D–F depict the model after being filled with iodine-based CT contrast medium. The presence of air in the acquisition performed on the empty model is evident (deep black areas), showing an appropriate interconnection between vessels without clogs. In contrast, the injection of the contrast medium into the model allowed the vascular phantom morphology (hyperintense white regions) to be clearly distinguishable from the surrounding water, characterized by a uniform grayscale. Moreover, the model resulted to be completely filled without the presence of air bubbles trapped into the structure. In both empty and contrast-filled cases, a mild gray level difference between the vessel's wall and the water bath was also visible. The AVM complex morphology and the nidus (marked with a cross in Fig. 4D–F) were faithfully reproduced with respect to the virtual 3D model (a quantitative comparison between the model and imaged phantom is reported in the Supplementary Information, see Figures S1 and S2).

Figure 5A and B shows photographs of the AVM structure embedded into the molded PDMS before and after injection of the contrast medium, respectively. In the PDMS replica, only the face of the box directly exposed to acetone vapors

resulted highly transparent, due to inevitable shadow effects affecting the inner side walls, which resulted in a higher roughness. However, the translucent appearance of the six lateral walls did not compromise the qualitative assessment of the phantom filling using the colored dye.

A 3D view of the system imaged into the anthropomorphic phantom head is shown in Figure 6A, whereas representative sagittal, coronal, and axial scans are shown in Figure 6B–D, respectively. The 3D model acceptably fitted the head support housing and, most importantly, depicted the precise nature of the compactness and location of the nidus in relation to the skull under the CT scanner. The good correspondence between the radiodensity of PDMS and brain matter coupled with the presence of the contrast medium emphasized the vessel's structure into the head support, providing a physical model accurately reproducing the clinical case anatomy. The 3D reconstruction of the AVM was then elaborated and compared with that derived from the patient. All the relevant vascular structures in our phantom could be clearly identified with a suitable level of morphological detail when compared with the target anatomy.

The patient AVM structure, the derived 3D model, and the reconstruction elaborated from the phantom CT scans are shown in Figure 7. The images of the model were positively evaluated by the two interventional radiologists with respect to the anatomical reproducibility of the phantom, compared with the patient case. We elaborated a survey that was submitted to the radiologists to have a quantitative evaluation of different features of the phantom. More in detail, they were asked to express their opinion on four different points (giving a score from 0 to 10 to each point) and converged to the following scoring: (1) morphological consistency between MAV source image and MAV phantom: 9; (2) imaging quality level (contrast, definition, etc.) of the MAV phantom with respect to the MAV source image: 9; (3) accuracy of the anatomical details reproduced in the MAV phantom: 7; (4) potential of the MAV phantom usage for surgical planning: 8.

A more detailed and quantitative comparative analysis between the 3D model derived from the patient and that reconstructed from the imaged AVM phantom is reported in the Supplementary Information.

Discussion

In the radiosurgery management of AVM, the accuracy of the target volume identification is crucial to ensure optimal treatment and avoid severe clinical complications. Target

contouring is a complex procedure, routinely performed with the aid of multimodal imaging and various data sets. 3D printed AVMs, as shown in Figure 7, offer an immediate and comprehensive visualization of the anatomy of the nidus, effectively supporting the lesional contouring task.

In this study, we selected a clinical case with a medium level of anatomical complexity in terms of AVM topology to validate our manufacturing approach using feasible tissue-equivalent materials. The procedure has potential to be extended to more complex abnormalities, for which the definition of a subset of vascular structures by the interventional radiologists is crucial for a functional reproduction of the AVM targeting as surgical purposes. In this sense, another patient-specific AVM characterized by a higher level of topological complexity with respect to the reported case study was produced by means of SLA and then CT scanned to assess the suitability of the proposed fabrication method to other clinical cases (see Figure S7, Section S3 in the Supporting Information). In this case, the part orientation with respect to the printing plate and the optimization of the supports configuration were more critical with respect to the case study reported. We observed from the CT scans that the AVM nidus and connected vessels could be fabricated with no channels clogging, indicating the reproducibility of the method in view of its application to more complex clinical situations.

The majority of the methods proposed for the fabrication of vascular phantoms in neurosurgery and radioneurosurgery mainly rely on sacrificial templating for the realization of vascular networks in silicone-based materials or on the direct fabrication of solid models representing the vessels.[29–34] Although the realization of complex vascular networks is critical for strategies based on the use of soluble 3D templates, a higher level of anatomical details and topological complexity is available for the direct manufacturing of vascular solid models. However, the lack of an internal channelization in these systems does not allow implementing functional and physiological features related to the circulation of fluids into the phantoms. Our integrated approach, based on SLA additive fabrication and casting of tissue-equivalent materials, offers the appropriate geometrical flexibility for the manufacturing of topologically complex structures, combining the fine reproduction of patient-specific anatomical details with radiographic response compatible with clinical CT imaging techniques.

The proposed method has potential to be optimized in terms of dimensional accuracy of the vascular phantom by using lower layer heights in conjunction with suitable additive fabrication strategies based on photopolymers able to contain the part manufacturing time (e.g., by using printing mechanisms that avoid the wiping step into the resin VAT). Another improvement to be taken into consideration to fabricate more realistic patient-specific phantoms is to preserve the correct spatial configuration of the AVM source anatomy into the anthropomorphic head support. When dealing with highly complex AVM topologies, the implementation of appropriate injection methods (e.g., based on automated fluid handling) to fill the vascular phantom with the contrast medium could be necessary to facilitate the system preparation and to avoid the inclusion of air bubbles.

A further development of this study could be the introduction of the real-time perfusion of the contrast medium into the phantom during CT imaging, to dynamically replicate the blood flow into the AVMs to investigate on different conditions for the contrast agent injection.

Conclusions

This study reported on the development of an efficient methodology for manufacturing a patient-specific vascular phantom for SRS applications. The system replicated the anatomical features of a brain AVMs. CT data acquired from a patient with this abnormality were selected to study representative clinical cases. The hollow vascular structure of the AVM was 3D reconstructed with image postprocessing techniques. The phantom was manufactured by fabricating the vessels by means of SLA, in combination with silicone casting to mimic the surrounding brain parenchyma. This physical model was produced using tissues-equivalent materials for radiology, previously tested under CT scans. The vascular system of the phantom was filled with a contrast agent usually employed on patients for CT imaging and radiologically validated.

The AVM phantom demonstrated to be an accurate morphological and functional model representing patient-specific anatomy information, appropriately matching the CT imaging obtained from the patient. The validation of this fabrication approach suggests that this kind of 3D cerebrovascular phantoms can be an enabling solution for SRS, such as surgical planning optimization, QA, and evaluation, with contrast-enhanced CT, of contrast uptake in small blood vessels.

Supplementary Material

Supplementary Data
Supplementary Figure S1
Supplementary Figure S2
Supplementary Figure S3
Supplementary Figure S4
Supplementary Figure S5
Supplementary Figure S6
Supplementary Figure S7
Supplementary Table S1

References

1. Doi K. Diagnostic imaging over the last 50 years: Research and development in medical imaging science and technology. Phys Med Biol 2006;51:R5–R27.
2. Tam MDBS. Building virtual models by postprocessing radiology images: A guide for anatomy faculty. Anat Sci Educ 2010;3:261–266.
3. Knisely JPS, Apuzzo MLJ. Historical aspects of stereotactic radiosurgery: Concepts, people, and devices. World Neurosurg 2019;130:593–607.
4. Ding C, Saw CB, Timmerman RD. Cyberknife stereotactic radiosurgery and radiation therapy treatment planning system. Med Dosim 2018;43:129–140.
5. Zhang XQ, Shirato H, Aoyama H, *et al.* Clinical significance of 3D reconstruction of arteriovenous malformation using digital subtraction angiography and its modification

with CT information in stereotactic radiosurgery. Int J Radiat Oncol Biol Phys 2003;57:1392–1399.

6. Chin LS, Regine WF. Principles and practice of stereotactic radiosurgery. Springer, Berlin, Germany. 2015;3:25–30.

7. Chávez GDRC, De Salles AAF, Solberg TD, et al. Three-dimensional fast imaging employing steady-state acquisition magnetic resonance imaging for stereotactic radiosurgery of trigeminal neuralgia. Neurosurgery 2005;56:E628–E636.

8. Fiehler J, Grzyska U. Pathophysiology and treatment of brain AVMs. Clin Neuroradiol 2009;19:82–90.

9. Qiu K, Haghiashtiani G, McAlpine MC. 3D printed organ models for surgical applications. Annu Rev Anal Chem (Palo Alto Calif) 2018;11:287–306.

10. Kim GB, Lee S, Kim H, et al. Three-dimensional printing: Basic principles and applications in medicine and radiology. Korean J Radiol 2016;17:182–197.

11. Mitsouras D, Liacouras P, Imanzadeh A, et al. Medical 3D printing for the radiologist. Radiographics 2015;35:1965–1988.

12. Pugliese L, Marconi S, Negrello E, et al. The clinical use of 3D printing in surgery. Updates Surg 2018;70:381–388.

13. Waran V, Narayanan V, Karuppiah R, et al. Utility of multimaterial 3D printers in creating models with pathological entities to enhance the training experience of neurosurgeons: Technical note. J Neurosurg 2014;120:489–492.

14. Levine ZH, Peskin AP, Holmgren AD, et al. Preliminary X-ray CT investigation to link Hounsfield unit measurements with the International System of Units (SI). PLoS One 2018;13:e0208820–e0208837.

15. Forte AE, Galvan S, Manieri F, et al. A composite hydrogel for brain tissue phantoms. Mater Des 2016;112:227–238.

16. Wang X, Meier D, Taguchi K, et al. Material separation in X-ray CT with energy resolved photon-counting detectors. Med Phys 2011;38:1534–1546.

17. Najafi M, Teimouri J, Shirazi A, et al. Technical note: Construction of heterogeneous head phantom for quality control in stereotactic radiosurgery. Med Phys 2017;44:5070–5074.

18. Jeong HS, Han Y, Kum O, et al. Development and evaluation of a phantom for multi-purpose dosimetry in intensity-modulated radiation therapy. Nucl Eng Technol 2011;43:399–404.

19. Ploch CC, Mansi CSSA, Jayamohan J, et al. Using 3D printing to create personalized brain models for neurosurgical training and preoperative planning. World Neurosurg 2016;90:668–674.

20. Nagassa RG, McMenamin PG, Adams JW, et al. Advanced 3D printed model of middle cerebral artery aneurysms for neurosurgery simulation. 3D Print Med 2019;5:11–22.

21. Zheng JP, Li CZ, Chen GQ. Multimaterial and multicolor 3D-printed model in training of transnasal endoscopic surgery for pituitary adenoma. Neurosurg Focus 2019;47:E21–E28.

22. Randazzo M, Pisapia J, Singh N, et al. 3D Printing in neurosurgery: A systematic review. Surg Neurol Int 2016;7:S801–S809.

23. Liu Y, Gao Q, Du S, et al. Fabrication of cerebral aneurysm simulator with a desktop 3D printer. Sci Rep 2017;7:44301–44313.

24. Wang JL, Yuan ZG, Qian GL, et al. 3D printing of intracranial aneurysm based on intracranial digital subtraction angiography and its clinical application. Medicine (Baltimore) 2018;97:e11103–e11108.

25. Lau I, Squelch A, Wan Y, et al. Patient-specific 3D printed model in delineating brain glioma and surrounding structures in a pediatric patient. Digit Med 2017;3:86–92.

26. Wurm G, Lehner M, Tomancok B, et al. Cerebrovascular biomodeling for aneurysm surgery: Simulation-based training by means of rapid prototyping technologies. Surg Innov 2011;18:294–306.

27. Amili O, Schiavazzi D, Moen S, et al. Hemodynamics in a giant intracranial aneurysm characterized by in vitro 4D flow MRI. PLoS One 2018;13:e0188323–e0188347.

28. Conti A, Pontoriero A, Iatì G, et al. 3D-printing of arteriovenous malformations for radiosurgical treatment: Pushing anatomy understanding to real boundaries. Cureus 2016;8:e594–e605.

29. Thawani JP, Pisapia JM, Singh N, et al. Three-dimensional printed modeling of an arteriovenous malformation including blood flow. World Neurosurg 2016;90:675–683.

30. Cogswell PM, Rischall MA, Alexander AE, et al. Intracranial vasculature 3D printing: Review of techniques and manufacturing processes to inform clinical practice. 3D Print Med 2020;6:18–30.

31. Lan Q, Chen A, Zhang T, et al. Development of three-dimensional printed craniocerebral models for simulated neurosurgery. World Neurosurg 2016;91:434–442.

32. Pucci JU, Christophe BR, Sisti JA, et al. Three-dimensional printing: Technologies, applications, and limitations in neurosurgery. Biotechnol Adv 2017;35:521–529.

33. Chueh JY, Wakhloo AK, Gounis MJ. Neurovascular modeling: Small-batch manufacturing of silicone vascular replicas. Am J Neuroradiol 2009;30:1159–1164.

34. Lim J, Kim AR, Kim S, et al. A new dip coating method using supporting liquid for forming uniformly thick layers on serpentine 3D substrates. Adv Mater Interfaces 2019;6:1901485–1901494.

35. Dong M, Chen G, Qin K, et al. Development of three-dimensional brain arteriovenous malformation model for patient communication and young neurosurgeon education. Br J Neurosurg 2018;32:646–649.

36. Dong M, Chen G, Li J, et al. Three-dimensional brain arteriovenous malformation models for clinical use and resident training. Medicine (Baltimore) 2018;97:e9516–e9520.

37. Rolland JP, Hagberg EC, Denison GM, et al. High-resolution soft lithography: Enabling materials for nanotechnologies. Angew Chem Int Ed Engl 2004;3:5796–5799.

38. Hwang Y, Candler RN. Non-planar PDMS microfluidic channels and actuators: A review. Lab Chip 2017;17:3948–3959.

39. Hoffmann T, Klink F, Boese A, et al. Development of a skull phantom for the assessment of implant X-ray visibility. Curr Dir Biomed Eng 2016;2:351–354.

40. Maiorano G, Mele E, Frassanito MC, et al. Ultra-efficient, widely tunable gold nanoparticle-based fiducial markers for X-ray imaging. Nanoscale 2016;8:18921–18927.

41. Adams F, Qiu T, Mark A, et al. Soft 3D-printed phantom of the human kidney with collecting system. Ann Biomed Eng 2017;45:963–972.

Address correspondence to:
Tommaso Santaniello
CIMAINA and Department of Physics
University of Milano
Via Celoria 16
Milan 20133
Italy

E-mail: tommaso.santaniello@unimi.it